Gyrokinetic simulations of magnetic reconnection

M. J. Pueschel,[1,2] F. Jenko,[1] D. Told,[1] and J. Büchner[2]
[1]*Max-Planck-Institut für Plasmaphysik, EURATOM Association, Garching D-85748, Germany*
[2]*Max-Planck-Institut für Sonnensystemforschung, Katlenburg-Lindau D-37191, Germany*

(Received 25 July 2011; accepted 7 October 2011; published online 1 November 2011)

Fast magnetic reconnection, believed to be a mechanism for rearranging the magnetic topology and creating energetic particles in many astrophysical and laboratory plasmas, is investigated with the nonlinear gyrokinetic code GENE. After some code-code benchmarking, extensive linear studies are presented, covering all relevant parameter dependencies of two-dimensional slab reconnection. The results are used to ascertain the validity of a fluid model and understand for which parameters it fails to describe the physics correctly. The nonlinear phase is studied for two scenarios: decaying and driven turbulence. In the former case, the initially injected energy is cascading towards the largest scales of the system, whereas a fully turbulent, quasi-stationary state develops if the system is driven through a Krook-type term in the gyrokinetic Vlasov equation. © *2011 American Institute of Physics*. [doi:10.1063/1.3656965]

I. INTRODUCTION

Fast magnetic reconnection—a process relevant for a number of both astrophysical and laboratory plasma effects—provides an efficient mechanism for releasing magnetic energy. Unlike Sweet–Parker[1,2] reconnection, its underlying physics involves collisionless effects and its characteristic time scale is the Alfvén time. For more information on these reconnection regimes, see Ref. 3 and references therein.

While elaborate work has been performed with fluid-based models (see, e.g., Refs. 4–8 for some more recent publications), kinetic aspects of fast reconnection require independent confirmation of the results obtained through such approaches. Thus, kinetic or gyrokinetic simulations are necessary to confirm the validity of reduced descriptions and expand upon them where such descriptions break down. A moderate number of gyrokinetic studies have been published.[9–12] The present work aims to cover all relevant parameter dependencies where the (linear) reconnection rate is concerned and to present examples of (nonlinear) reconnection turbulence while focusing on particle acceleration and magnetic structure formation.

The paper is organized as follows. First, a brief description of the reduced gyrokinetic equations is provided, as well as of the GENE code which was used to obtain the numerical results in this work. As it constitutes the physical driving mechanism, the current sheet initial condition is detailed, and successful benchmarking with a previous publication is demonstrated. Linear simulation results are then compared to analytical theory, followed by nonlinear investigations for both decaying and driven turbulence. Lastly, the findings are summarized.

II. NUMERICAL APPROACH

A. The gyrokinetic equations

Gyrokinetic theory[13–15] reduces the six-dimensional phase space by one dimension through elimination of the fast gyrating motion of particles about magnetic field lines. As a consequence, its applicability is limited to strong guide fields and physical time scales slower than the gyration time. In particular, effects like light waves and compressional Alfvén waves are not captured, while many aspects relevant to fast magnetic reconnection are included in this description. A typical formulation[16,17] of the local gyrokinetic Vlasov equation for the perturbed particle distribution function f_j of species j reads

$$\begin{aligned}
&\frac{\partial g_j}{\partial t}+\frac{1}{B_{\rm ref}}\frac{B_0}{B_{0\|}^*}\left(\frac{\mu B_0}{m_j\Omega_j}+\frac{v_\|}{\Omega_j}\right)\left[\left(\frac{\partial B_0}{\partial x}-\kappa_2\frac{\partial B_0}{\partial z}\right)\Gamma_{jy}\right.\\
&\quad\left.-\left(\frac{\partial B_0}{\partial y}+\kappa_1\frac{\partial B_0}{\partial z}\right)\Gamma_{jx}\right]+\frac{B_{\rm ref}}{JB_0}v_\|\Gamma_{jz}\\
&\quad-\frac{F_{j0}}{B_{\rm ref}}\frac{B_0}{B_{0\|}^*}\left[L_n^{-1}+\left(\frac{m_jv_\|^2}{2T_{j0}}+\frac{\mu B_0}{T_{j0}}-\frac{3}{2}\right)L_{Tj}^{-1}\right]\\
&\quad\times\left[c\frac{\partial\chi}{\partial y}+\left(\frac{v_\|^2}{\Omega_j}+\frac{\mu B_0}{m_j\Omega_j}\right)\left(\frac{\partial B_0}{\partial y}+\kappa_1\frac{\partial B_0}{\partial z}\right)\right]\\
&\quad+\frac{1}{B_{\rm ref}}\frac{B_0}{B_{0\|}^*}\frac{4\pi v_\|^2}{B_0\Omega_j}\frac{\partial p_{j0}}{\partial x}\Gamma_{jy}-\frac{B_{\rm ref}}{JB_0}\frac{\mu}{m_j}\frac{\partial B_0}{\partial z}\frac{\partial f_j}{\partial v_\|}\\
&\quad+\frac{cF_{j0}}{B_{\rm ref}}\frac{B_0}{B_{0\|}^*}\left(\frac{\partial\chi}{\partial x}\Gamma_{jy}-\frac{\partial\chi}{\partial y}\Gamma_{jx}\right)=\left.\frac{\partial f_j}{\partial t}\right|_{\rm coll},
\end{aligned}\tag{1}$$

with the modified distribution function $g_j=f_j-[q_j/(m_jc)]\bar{A}_{1\|}\partial F_{j0}/\partial v_\|$; the generalized potential $\chi_j=\bar{\phi}-(v_\|/c)\bar{A}_{1\|}+(\mu/q_j)\bar{B}_{1\|}$, where bars denote gyroaverages; the background magnetic field B_0, with $B_{0\|}^*=B_0+B_0 2\pi m_j v_{Tj}/(q_jB_0^2)v_\| j_{0\|}$; and the curvature coefficients (defined via the metric g): $\kappa_k=(g^{1k}g^{23}-g^{2k}g^{13})/(g^{11}g^{22}-g^{21}g^{12})$. Furthermore, t denotes time, $B_{\rm ref}$ the reference magnetic field, F_{j0} the background distribution function, c the speed of light, e the elementary charge, q_j, m_j, n_{j0}, T_{j0}, and Ω_j the charge, mass, background density, background temperature, and gyration frequency of species j, respectively, J the Jacobian, and p_{j0} the background pressure. L_n and L_{Tj} are the background gradient lengths of n_{j0} and T_{j0}, respectively. The quantities Γ_{jk} are defined to be $\partial_k g_j-[(q_j/m_jv_\|)]\partial_k\chi_j\partial_{v_\|}F_{j0}+[(q_j/m_jc)]\bar{A}_{1\|}\partial_k\partial_{v_\|}F_{j0}$. The symbols x, y, z, $v_\parallel$, and μ denote the radial, binormal, parallel, parallel velocity, and magnetic moment coordinate, respectively.

The electromagnetic fields Φ, $A_\parallel$, and $B_\parallel$ are evaluated self-consistently through the field equations, of which the equations for Φ and $B_\parallel$ constitute a coupled set.

$$\Phi = \frac{\mathcal{C}_3\mathcal{M}_{00} - \mathcal{C}_2\mathcal{M}_{01}}{\mathcal{C}_1\mathcal{C}_3 - \mathcal{C}_2^2}, \tag{2}$$

$$B_\parallel = \frac{\mathcal{C}_1\mathcal{M}_{01} - \mathcal{C}_2\mathcal{M}_{00}}{\mathcal{C}_1\mathcal{C}_3 - \mathcal{C}_2^2}, \tag{3}$$

$$A_\parallel = \left(\sum_j \frac{8\pi^2 q_j B_0}{m_j c}\int v_\parallel J_0 g_j \mathrm{d}v_\parallel \mathrm{d}\mu\right) \times \left(k_\perp^2 + \sum_j \frac{8\pi^2 q_j^2 B_0}{m_j c^2 T_{j0}}\int v_\parallel^2 J_0^2 F_{j0}\mathrm{d}v_\parallel \mathrm{d}\mu\right)^{-1}, \tag{4}$$

with the abbreviations

$$\mathcal{M}_{00} = \sum_j \frac{2q_j}{m_j}\pi B_0 \int J_0 f_j \mathrm{d}v_\parallel \mathrm{d}\mu, \tag{5}$$

$$\mathcal{M}_{01} = \sum_j \frac{q_j \pi (2B_0/m_j)^{3/2}}{ck_\perp}\int \mu^{1/2} J_1 f_j \mathrm{d}v_\parallel \mathrm{d}\mu, \tag{6}$$

$$\mathcal{C}_1 = \frac{k_\perp^2}{4\pi} + \sum_j \frac{q_j^2 n_{j0}}{T_{j0}}(1-\Gamma_0), \tag{7}$$

$$\mathcal{C}_2 = -\sum_j \frac{q_j n_{j0}}{B_0}(\Gamma_0 - \Gamma_1), \tag{8}$$

$$\mathcal{C}_3 = -\frac{1}{4\pi} - \sum_j \frac{m_j n_{j0} v_{Tj}}{B_0^2}(\Gamma_0 - \Gamma_1), \tag{9}$$

where $\Gamma_k = I_k(b)\,\mathrm{e}^{-b}$ is defined through the modified Bessel function I_k of argument $b = v_{Tj}^2 k_\perp^2/(2\Omega_j^2) = T_{j0}k_\perp^2/(m_j\Omega_j^2)$; $k_\perp$ is the perpendicular wave vector and J_k is the Bessel function of argument $(2\mu B_0/m_j)^{1/2}k_\perp/\Omega_j$.

Below, the Vlasov equation is reduced to the two-dimensional slab geometry employed in this work and normalized to GENE units.

B. The GENE code

The above equations are solved with the GENE code.[17] In its radially local version—which is used throughout this work—it operates on Fourier space in the perpendicular directions x and y, while for the purpose of investigating two-dimensional spatial domains, the coordinate z parallel to the guide field is not resolved. The velocity space uses equidistant grid points in $v_\parallel$ and a weighed Gauss-Legendre grid in μ. Here, it is run in nonlinear initial value solving mode and slab geometry, with the collision[16,17] and $v_\parallel$ hyperdiffusion[18] terms turned on where specified.

The parallel dynamics are now neglected—i.e., $\partial_z f = 0$ for any physical quantity f—and a homogeneous background field B_0 is assumed. Additionally, an option for reconnection drive is added through a Krook-type term which forces the system toward the initial state with an unstable current sheet. With these modifications, the normalized gyrokinetic Vlasov equation as employed throughout this work becomes[16,17]

$$\frac{\partial g_j}{\partial t} = -\left[\omega_n + \left(v_\parallel^2 + \mu B_0 - \frac{3}{2}\right)\omega_{Tj}\right]F_{j0} i k_y \chi + \sum_{\vec{k}'}(k_x' k_y - k_x k_y')\chi(k')g_j(k-k') - \omega_{\mathrm{Kr}}\|g_{j,ky=0}(t) - g_{j,ky=0}(t=0)\| + \epsilon_{\mathrm{v}\parallel}\left(\frac{\Delta v_\parallel}{2}\frac{\partial}{\partial v_\parallel}\right)^4 g_j + \left.\frac{\partial f_j}{\partial t}\right|_{\mathrm{coll}}, \tag{10}$$

with the modified distribution function $g_j = f_j + 2q_j v_\parallel \bar{A}_{\parallel j} F_{j0}/(m_j v_{Tj})$, the background distribution $F_{j0} = \pi^{-3/2}\exp(-v_\parallel^2 - \mu B_0)$, the generalized potential $\chi = \bar{\phi}_j - v_{Tj} v_\parallel \bar{A}_{\parallel j} + (T_{j0}/q_j)\mu \bar{B}_{\parallel j}$, and the normalized gradients $\omega_k = L_{\mathrm{ref}}/L_k$ defined relative to the macroscopic reference length L_{ref}. The quantities ω_{Kr} and $\epsilon_{\mathrm{v}\parallel}$ denote, respectively, the Krook drive strength and the $v_\parallel$ hyperdiffusion coefficient. Note that the Krook term is similar to what can be found in Ref. 19, only in the present paper, the pseudo-equilibrium is simply the initial condition $g_{j,ky=0}(t=0)$. Thus, the term constantly forces the system towards that initial condition, re-injecting energy that is lost through dissipative processes, e.g., hyperdiffusion or collisions.

The normalized field equations read

$$\Phi = \frac{\mathcal{C}_3\mathcal{M}_{00} - \mathcal{C}_2\mathcal{M}_{01}}{\mathcal{C}_1\mathcal{C}_3 - \mathcal{C}_2^2}, \tag{11}$$

$$B_\parallel = \frac{\mathcal{C}_1\mathcal{M}_{01} - \mathcal{C}_2\mathcal{M}_{00}}{\mathcal{C}_1\mathcal{C}_3 - \mathcal{C}_2^2}, \tag{12}$$

$$A_\parallel = \left(\sum_j \frac{1}{2} q_j n_{j0} v_{Tj}\beta\pi B_0 \int v_\parallel J_0 g_j \mathrm{d}v_\parallel \mathrm{d}\mu\right) \times \left(k_\perp^2 + \sum_j \frac{q_j^2 n_{j0}}{m_j}\beta\pi B_0 \int v_\parallel^2 J_0^2 F_{j0}\mathrm{d}v_\parallel \mathrm{d}\mu\right)^{-1}, \tag{13}$$

$$\mathcal{M}_{00} = \sum_j q_j n_{j0}\pi B_0 \int J_0 g_j \mathrm{d}v_\parallel \mathrm{d}\mu, \tag{14}$$

$$\mathcal{M}_{01} = \sum_j q_j n_{j0}\pi B_0^{3/2}\frac{v_{Tj}}{k_\perp}\int \mu^{1/2} J_1 g_j \mathrm{d}v_\parallel \mathrm{d}\mu, \tag{15}$$

$$\mathcal{C}_1 = k_\perp^2 \lambda_D^2 + \sum_j \frac{q_j^2 n_{j0}}{T_{j0}}(1-\Gamma_0), \tag{16}$$

$$\mathcal{C}_2 = -\sum_j \frac{q_j n_{j0}}{B_0}(\Gamma_0 - \Gamma_1), \tag{17}$$

$$\mathcal{C}_3 = -\frac{2}{\beta} - \sum_j \frac{2n_{j0}T_{j0}}{B_0^2}(\Gamma_0 - \Gamma_1), \tag{18}$$

where $\beta = \beta_{\mathrm{e}} = 8\pi n_{\mathrm{e}0} T_{\mathrm{e}0}/B_{\mathrm{ref}}^2$ and $\lambda_{\mathrm{D}} = B_{\mathrm{ref}}/(4\pi c^2 n_{\mathrm{e}0} m_{\mathrm{i}})^{-1/2}$.

In cases where the gradient drive, Krook, hyperdiffusion, and collision terms are turned off, this system is preserving energy to machine precision,[20] a fact that becomes relevant for cases of decaying turbulence discussed later. It should also be noted that GENE is a massively parallel code, a necessity for running the type of simulations shown in the present work where runs were performed on up to 4096 cores.

For the linear simulation results, extensive convergence tests were performed to ensure physicality of the growth rate. Typical resolutions were 48–96 points resolving $|v_\parallel| \leq 3v_{Tj}$ and 8–16 points resolving $\mu \leq 9v_{Tj}^2$, where $v_{Tj} = (2T_j/m_j)^{1/2}$, with the radial resolution strongly depending on the set of physical parameters, ranging from $N_x = 96$–16384. The numerically challenging nature of the turbulence simulations, however, makes such encompassing tests unfeasible, which is why convergence checks were performed only in the spatial domain—i.e., $N_{x,y}$ and $L_{x,y}$—for those cases.

C. Current sheet implementation

Through the initial condition, free energy is injected into the system. In cases with the Krook term turned off, this happens only at the beginning of the simulation, while an active Krook term continuously provides energy which is eventually dissipated through $v_\parallel$ hyperdiffusion.

The current sheet initial condition in GENE works as follows. First, a homogeneous density is set up, with a small perturbation of equal amplitude and random phase added to all finite k_y modes. Then, the velocity space is added, based on one of three options in $x - v_\parallel$ space (see Fig. 1): by default, the Maxwellian distribution is shifted by $-v_{\rm shift}\cos(k_x x N_{\rm xp})$, with the number of sinusoidal periods in the x direction $N_{\rm xp}$ usually set to one (exception: turbulence simulations); alternatively, the shift profile may be composed of two Gaussians with opposite sign, with a small offset subtracted to ensure continuity at $x = \pm L_x/2$, 0 (where the Gaussians have fallen off to $< 2 \times 10^{-3}$); or, by contrast, $v_\parallel \sin(k_x x)$ is simply multiplied onto an unshifted Maxwellian. The last option is identical[21] to the setup of the initial condition in Ref. 11. It needs to be stressed that, in the first two cases, where $v_{\rm shift}$ is a free parameter, its value determines the resulting growth rate γ. By normalizing γ to the inverse Alfvén time $\gamma_A \propto B_y(t=0) \propto v_{\rm shift}$, this dependency is eliminated, however.

It is to be noted that all these profiles are periodic—with the consequence that there are always an even number of current sheets in the system. While in many previous investigations, Harris sheets[22] have been studied, periodic profiles are a popular alternative and prove to be a more convenient setup in GENE.

D. Benchmarking

In Ref. 11, linear k_y spectra for fast reconnection have been calculated and were later corrected[23] as a result of a fruitful collaboration between the authors of Ref. 11 and the present paper. Here, both data from that publication—obtained with the GS2/AstroGK code[24]—and GENE results are shown for four different parameter sets. Throughout this work, the normalization

$$\gamma \rightarrow \gamma\gamma_{\rm A} = \gamma \frac{k_x B_{y0,\max}}{\sqrt{n_{e0} m_i}} \sqrt{\frac{2}{\beta}} \tag{19}$$

is employed.

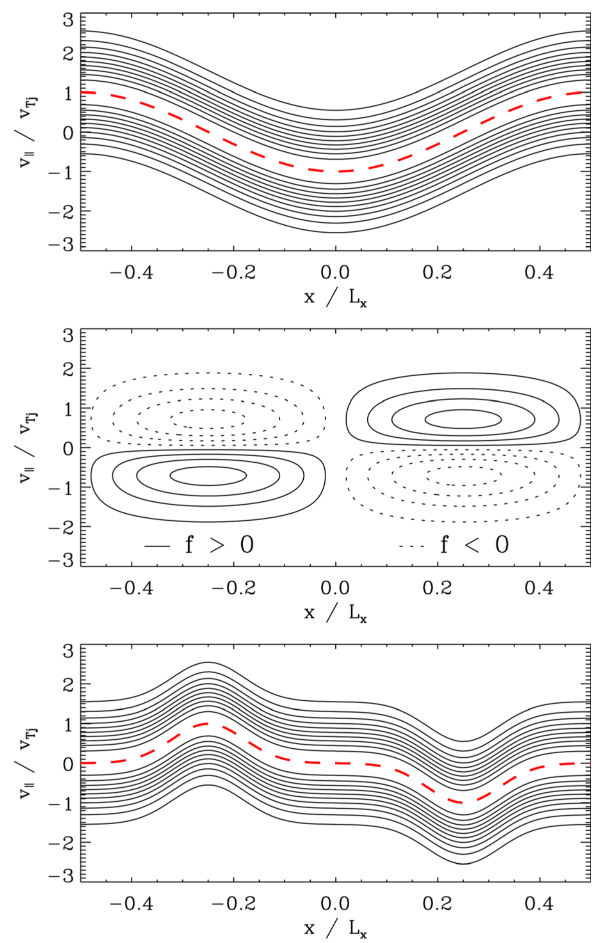

FIG. 1. (Color online) From top to bottom, the three initial conditions $f(t=0)$ are illustrated in the $x - v_\parallel$ plane (see the text): the default $v_\parallel$-shifted Maxwellian, a $v_\parallel$-multiplied Maxwellian, and a Gaussian-shifted Maxwellian. The red dashed lines indicate the ridge of maxima for the shifted cases; only for the second setup does f include negative values.

The growth rate spectra in Fig. 2 correspond to a case with $k_x = 0.2$, reduced mass ratio $m_e/m_i = 0.01$, and plasma pressure $\beta = 0.2$, with results shown for temperature ratios $T_i/T_e = 2 \times 10^{-4}$ and $T_i/T_e = 5$. A slightly different case is shown in Fig. 3, where $m_e/m_i = 0.04$ and plasma pressure

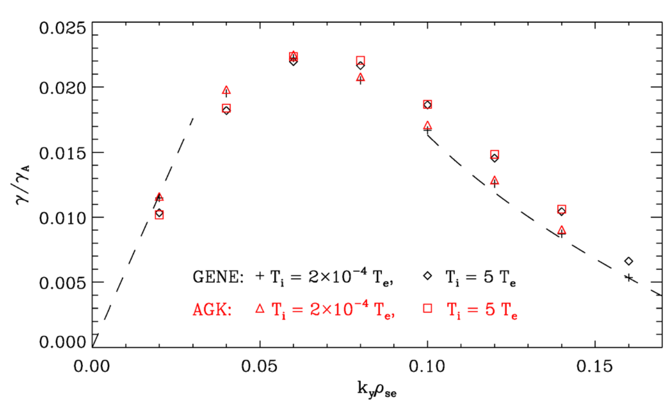

FIG. 2. (Color online) Linear benchmark between GENE (black crosses and diamonds) and GS2/AGK (red triangles and squares) for two different temperature ratios, with the value for the latter taken from Refs. 11 and 23. For the case shown here, $\beta = 0.2$ and $m_e/m_i = 0.01$. The two dashed lines correspond to fluid model limits, with the assumption $T_i = 0$ made to achieve agreement (see also Sec. III B 4 in the text).

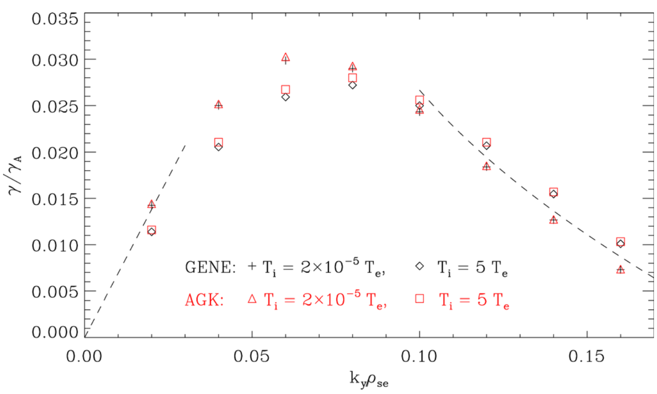

FIG. 3. (Color online) Linear benchmark between Gene (black crosses and diamonds) and GS2/AGK (red triangles and squares) for two different temperature ratios, with the value for the latter taken from Refs. 11 and 23. For the case shown here, $\beta = 0.3$ and $m_e/m_i = 0.04$. The dashed lines correspond to two fluid model limits, with the assumption $T_i = 0$ made to achieve agreement (see also Sec. III B 4 in the text).

$\beta = 0.3$. The temperature ratios are essentially identical to those in Fig. 2. Clearly, there is excellent quantitative agreement between the codes, with relative deviations of the growth rate never exceeding four percent.

Using these encouraging benchmark results as a starting point, linear studies were performed with the above parameters as a base case: $m_e/m_i = 0.04$, $\beta = 0.3$, and $k_x = 0.2$; choosing a default ion temperature setting of $T_i = T_e$. Below, the results of these investigations are presented, as are comparisons with a standard analytical model.

III. LINEAR PHYSICS

A. Analytical fluid model

Ref. 25 contains an analytical fluid model, along with solutions of the dispersion relation, which has since been used as a kind of standard model in various studies. For small gyroradii, an adiabatic equation of state for the electrons is used, while in the large gyroradii case—which is of relevance to the present work—an isothermal limit is assumed and use is made of the Padé approximation. More recently, the model has been adapted in Ref. 11, yielding expressions for the normalized linear growth rates in the following limits:

$$k_y \to 0: \quad \gamma = \left(\frac{2}{\pi}\right)^{1/3} k_y \left(\frac{m_e}{m_i}\frac{2}{\beta_e}\right)^{1/6} \left(1 + \frac{T_i}{T_e}\right)^{1/3}, \tag{20}$$

$$k_y \to k_x: \quad \gamma = \frac{2k_y\sqrt{k_x^2 - k_y^2}}{\pi}\left(\frac{m_e}{m_i}\frac{2}{\beta_e}\right)^{1/2} \times \left(1 + \frac{T_i}{T_e}\right)^{1/2} \tan\frac{\pi\sqrt{1 - k_y^2/k_x^2}}{2}. \tag{21}$$

In terms of the stability parameter[26] $\Delta' = 2(k_x^2 - k_y^2)^{1/2} \times \tan[(1 - k_y^2/k_x^2)^{1/2}\pi/2]$, these limits correspond to $\Delta' \to \infty$ and $\Delta' \to 0$, respectively.

The validity of those expressions requires, however, that the following limits are fulfilled (here, $\beta_{tot} = \beta_e + \beta_i$ is the total plasma pressure):

$$\left(1 + \frac{T_i}{T_e}\right)\rho_s^2 \gg d_e^2 \quad \Leftrightarrow \quad \beta_{tot} \gg 2\frac{m_e}{m_i}, \tag{22}$$

with the sound speed gyroradius $\rho_s \equiv \rho_{se}$ and the electron skin depth d_e, corresponding to a region where the electrons behave isothermally rather than adiabatically;[25] and

$$\left(1 + \frac{T_i}{T_e}\right)\rho_e^2 \ll \left(\frac{d_e}{k_y}\gamma\right)^2 \quad \Leftrightarrow \quad \beta_{tot} \ll 2\frac{k_y^2}{\gamma^2} = 2\left(\frac{m_e}{m_i}\right)^{1/4}, \tag{23}$$

where ρ_e is the electron gyroradius, and the last substitution can be made by making use of the small-k_y limit in Eq. (20). This second condition is a combination of two prerequisites, where both the electron polarization drift and finite Larmor radius (FLR) effects may be neglected (see Ref. 11).

In combination, the above limits set a range of applicability for β_{tot} through the choice of mass ratio. For the parameters used in Sec. II D—which constitute a standard set throughout this work—they are only marginally fulfilled. The remainder of this work contains multiple instances where small changes to those parameters quickly lead to the fluid model becoming inapplicable.

With the model equations in mind, the focus is now turned to direct gyrokinetic simulation results, where the applicability and limitations of said equations can be tested.

B. Simulation results

1. Radial wave number

The radial wave number k_x enters the model equations only in combination with k_y. A major aspect of its influence on the growth rate spectra is that the range of unstable k_y is given by $[0, k_x]$. As can be seen in Fig. 4 (where the abscissa employs a rescaled $\bar{k}_y = k_y(0.2/k_x)$, stretching curves for different k_x values to the same width), this behavior is reflected by the simulation results. Moreover, up to the point where $k_\perp \gtrsim 1$, there is excellent agreement between fluid theory and the gyrokinetic growth rates. The deviation at high $k_\perp$ is to be expected, as finite Larmor radius effects start to

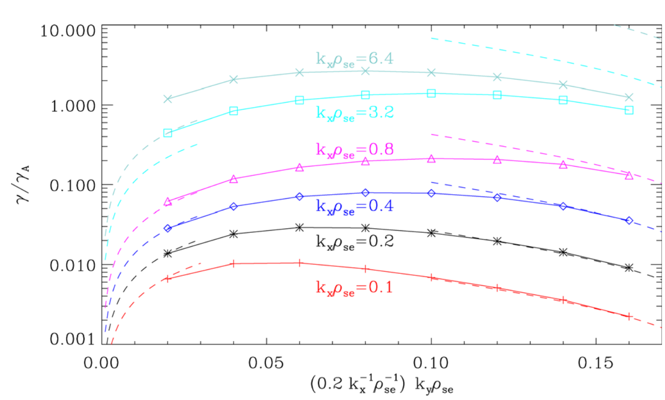

FIG. 4. (Color online) Linear scan of the radial wavenumber k_x. Since the unstable k_y range varies with k_x, the abscissa is rescaled, with $\bar{k}_y = k_y(0.2/k_x)$. Comparison of the solid lines (simulation data) with the dashed lines (fluid model) reveals that only at very high k_x does the model start to break down. Note that $\rho_{se} = (T_e/m_i)^{1/2}/\Omega_i$.

become important which are captured by gyrokinetics but not by the fluid model.

2. Current profile

As there is a lot freedom with regard to the current sheet setup, a variety of different settings were studied to assess the universality of the results obtained with the standard configuration. It was found that—apart from the different normalization factor due to $B_{y0,max} \propto v_{shift}$—the (normalized) growth rates are independent of the current amplitude, as is to be expected. At higher v_{shift}, the parallel velocity space needs to be extended, however, impacting numerical requirements (with the highest value investigated being 3 in units of the thermal velocity).

Another degree of freedom stems from the fact that the current may be carried by either the electrons, the ions, or both species. Due to the different masses, a given (normalized) velocity shift will result in a different $B_{y0,\mathrm{max}}$ depending on the species properties, but the normalized reconnection rate is not influenced by these choices.

As mentioned previously in Sec. II C, using another sinusoidal current sheet implementation where $v_{\parallel}\sin(k_x x)$ is multiplied onto the Maxwellian also gives the same results as the standard configuration.

Fig. 5 compares growth rate spectra of those standard results with numbers obtained for a bi-Gaussian current profile, while all other parameters remained unchanged. Although there exist clear qualitative differences between the curves, they can be attributed to higher k_x components of the profile, see also the k_x investigation in Sec. III B 1—higher k_x contributions result in a spectral shift to higher k_y.

3. Mass ratio and β

As evidenced by Figs. 6 and 7, both the mass ratio dependence and the impact of β are captured relatively well by the model for the present parameter choices. Deviations are found only in Fig. 7 for small k_y, where Eq. (22) starts to fail once the β value is changed. To ensure that this is indeed the reason for the deviation—rather than a k_y that may still be

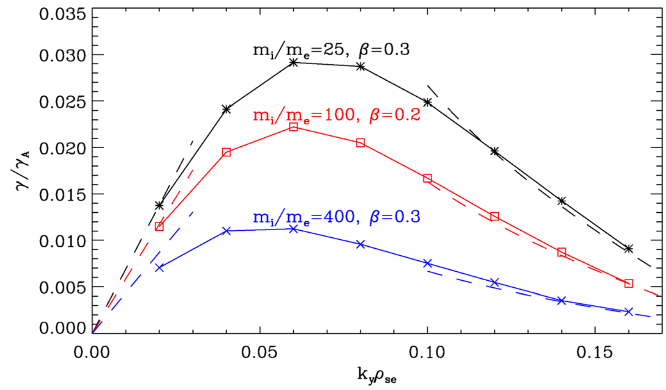

FIG. 6. (Color online) Linear scan over mass ratios. The numerical growth rates ($T_{\mathrm{i}} = T_{\mathrm{e}}$, solid lines) agree fairly well with the model predictions (dashed lines), however, only if the ions are assumed to be cold (see also Sec. III B 4 on the ion temperature and Ref. 11).

too large for the small-k_y limit to apply—additional points at very low k_y are shown in the $\beta = 1$ case, which clearly do not agree with the model predictions.

Since the fluid model puts certain constraints, namely Eqs. (22) and (23), on the total plasma β_{tot} rather than the electron β alone, a closer look at the ion temperature dependence will be taken next—note that for $T_{\mathrm{i}} \gg T_{\mathrm{e}}$, the relation $\beta_{\mathrm{tot}} \propto T_{\mathrm{i}}$ holds. There, it will be indicated that, to a certain degree, the agreement shown here is coincidental; and that the model does not, in general, predict the growth rates correctly, once its prerequisite limits are not fulfilled fairly exactly anymore.

4. Ion temperature

Previously, it has been conjectured that fluid theory and gyrokinetic reconnection rates disagree fundamentally with regard to the ion temperature dependence.[11] This intuition appears to be corroborated by a T_{i} scan (see Fig. 8) where clearly, the analytical curves show strong dependencies whereas the simulation data varies little with T_{i}.

With the findings of the previous β scan, however, additional parameter points were selected with significantly larger $m_{\mathrm{i}}/m_{\mathrm{e}}$ to extend the β_{tot} range where fluid theory is

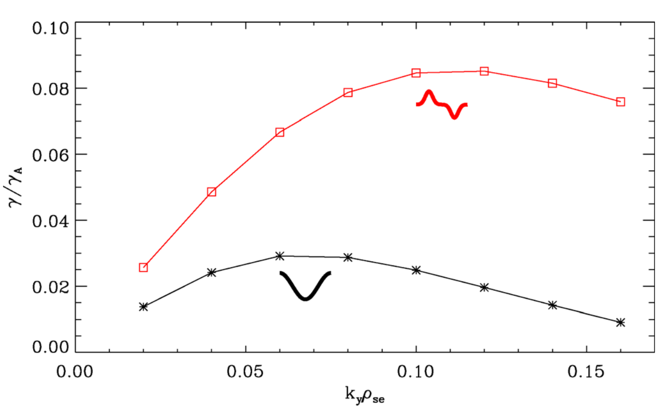

FIG. 5. (Color online) The curve marked by black stars is identical to the benchmark case (with $k_x = 0.2$, black crosses in Fig. 3), while red squares denote growth rates obtained with a bi-Gaussian current profile. Due to contributions of higher k_x, the latter stretches to higher k_y and also exhibits higher γ.

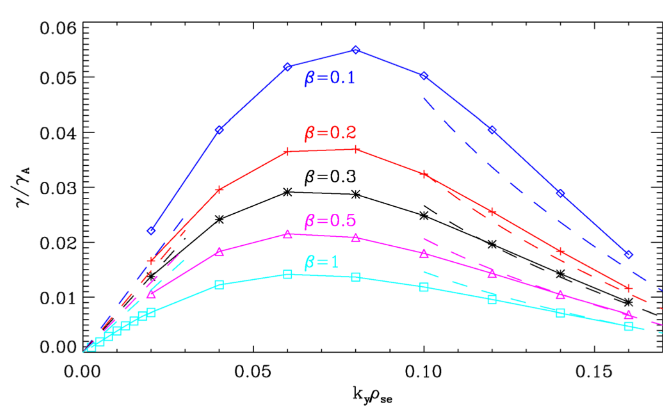

FIG. 7. (Color online) Linear growth rates for different values of the normalized plasma pressure $\beta = \beta_{\mathrm{e}}$ (solid curves). While in the limit of $k_y \to k_x$, the values agree reasonably well with the model predictions (dashed lines), deviations for both small and large β in the $k_y \to 0$ limit indicate that for the present parameters, the model is not fully applicable anymore.

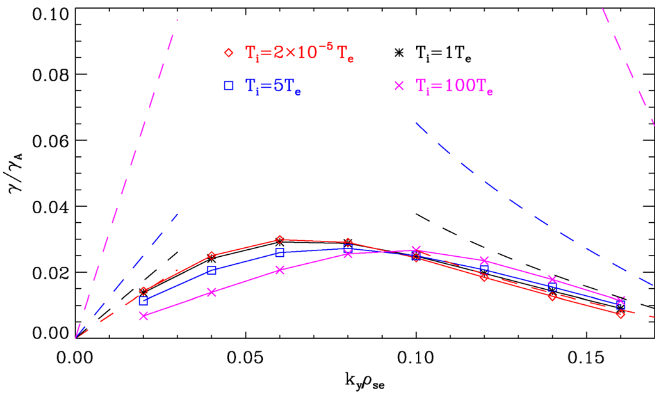

FIG. 8. (Color online) Study of the ion temperature dependence of the reconnection rate. The solid lines (simulations) show little variation over a large range of T_i, whereas a finite ion temperature quickly causes the dashed lines (model) to rise. The cause for this differing behavior lies in the violation of conditions involving $\beta_{tot}=\beta_{tot}(T_i)$ (see Eqs. (22) and (23) in the text).

applicable. The need for large mass ratios is a consequence of Eq. (22); for reduced and even hydrogen mass ratios, the applicability range with respect to the β and T_i values can be fairly narrow or even virtually nonexistent.

As shown in Fig. 9, the apparent disagreement between the fluid and the gyrokinetic model is thus resolved. The necessary mass ratios, however, stress the need for either extended theory or reliance on numerical simulations throughout wide ranges of the physical parameters β, T_i, and m_i/m_e, as not fulfilling condition (22) rather rigorously causes significant deviations when comparing theoretical predictions and simulation results.

5. Collisions

All above results were obtained in the collisionless limit. While one may generally be interested in studying fully collisional reconnection with different tools, the aim of this section is to look at the enhancement of the reconnection rate due to low but finite collisionality. As the results in Fig. 10

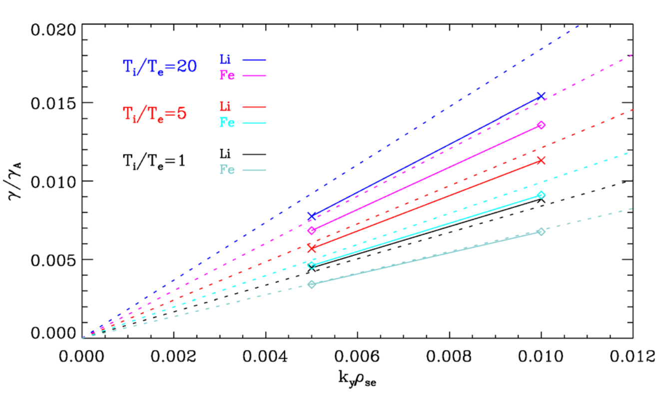

FIG. 9. (Color online) Additional ion temperature growth rates from simulations (solid lines) with adjusted parameters: Fe (diamonds) and Li (crosses) mass ratio results are shown and β is taken to be 0.001. With decreasing electron mass, the β range where the model (dashed curves) predicts the reconnection rate correctly is expanded. Note that, as the low-k_y range appears to be more sensitive with regard to differences between simulations and the model predictions in Eqs. (20) and (21)—see Fig. 7—only the $k_y \to 0$ limit is shown here.

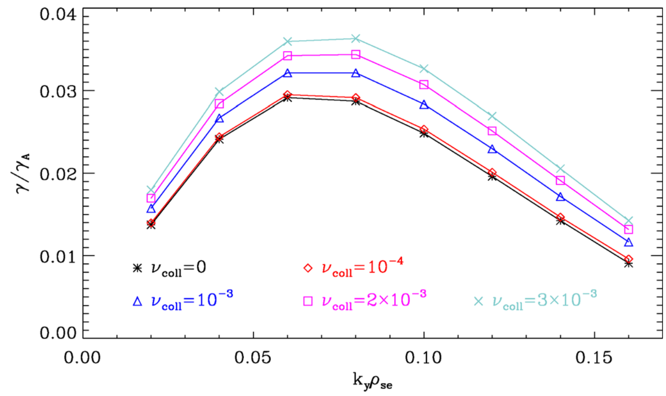

FIG. 10. (Color online) Reconnection rates in the presence of (low) collisionalities—for the definition of ν_{coll}, see the text. The destabilizing effect of collisions becomes clearly visible. Note that the growth rates have been rescaled to account for collision-borne changes to the driving current sheet, $B_{y0,max}=B_{y0,max}(t)$.

suggest, given a sufficiently low collision frequency (in Gaussian units),

$$\nu_{coll} = \frac{\pi \log_c e^4 n_0 L_{ref}}{2^{3/2} T_e^2}, \tag{24}$$

the nature of the reconnection does not change qualitatively.

It should be noted that the presence of collisions will, over time, erode the driving current sheet. As this typically leads to the drive being diminished significantly (i.e., by about 10%) during the time that the growth rate is averaged over, it becomes necessary to correct for this effect through taking $B_{y0,max}=B_{y0,max}(t)$.

At even higher $\nu_{coll} \gtrsim 10^{-2}$, the growth rates become very large (one to two orders of magnitude larger than the values shown here), accompanied by drastic changes to the growth rate spectra, hinting at new, collisional modes being destabilized. A proper investigation of these modes is left to future work. This still leaves a relatively large range of collisionalities—which overlaps with typical collisionalities in fusion plasmas—where one may safely assume moderate collisional enhancement of collisionless reconnection to be applicable.

Reference 25 predicts the collisional relative enhancement of the growth rate in two limits

$$\text{large } \rho_i: \qquad \gamma = \gamma_0 \left(1 + \frac{\nu_{ei}}{2\gamma}\right)^{1/6} \tag{25}$$

and

$$\text{small } \rho_i: \qquad \gamma = \gamma_0 \left(1 + \frac{\nu_{ei}}{2\gamma}\right)^{1/2}. \tag{26}$$

Here, ν_{ei} is the electron-ion collision frequency and γ_0 is the collisionless growth rate. It can be assumed, however, that including additional collision physics beyond ion-electron collisions—as done in GENE, where a Boltzmann operator (preserving particle number, energy, and momentum) with all types of binary collisions is used[16,17]—does not alter these results dramatically. Thus, for the purpose of this work, ν_{ei} is used interchangeably with the collision frequency $\nu_{\rm coll}$ in GENE. Note that the exponents (1/6 and 1/2) in the above equations are henceforth denoted by the symbol α_ν.

In the derivation of the model, use was made of an approximation $\rho_s^2 \gg d_e^2$, see Eq. (22). Thus, an exponent $\alpha_\nu = 1/6$ should be expected to apply for $k_y \to 0$. However, since the physical parameters have been shown not to fulfill this condition very rigorously, one may expect to see deviations from the predicted scaling.

In order to facilitate direct comparisons, $\nu_{\rm coll}$ is renormalized to the same units as the linear growth rate,

$$\nu_{\rm coll} \to \nu_{\rm coll} \frac{n_{\rm e}}{T_{\rm e}^2}\left(\frac{m_{\rm i}}{m_{\rm e}}\right)^{1/2}\frac{c_s}{L_{\rm ref}}. \tag{27}$$

Here, $c_s = (T_{\rm e}/m_{\rm i})^{1/2}$ is the normalized sound speed. Since the model predicts the *relative* enhancement of the growth rate, it is applied to the numerical results obtained for $\nu_{\rm coll} = 0$.

As shown in Fig. 11, the simulation data is well-described by a scaling exponent of $\alpha_\nu = 1/2$ for $k_y \to k_x$; whereas, in the limit of small k_y, it seems to follow an exponent of $\alpha_\nu = 1/3$ rather than the model prediction 1/6. This may be the consequence of small-$\rho_{\rm i}$ effects playing a role for the present choice of parameters.

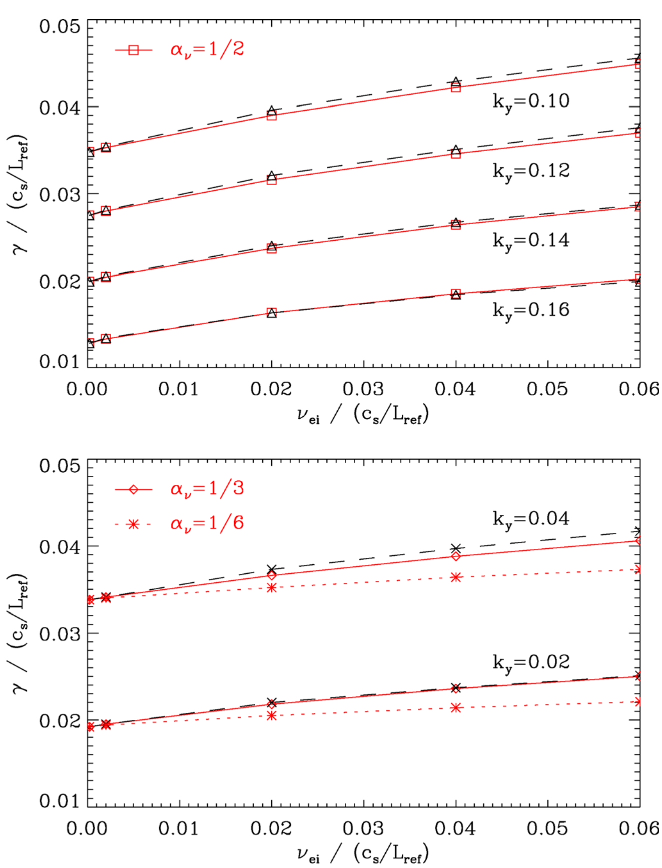

FIG. 11. (Color online) Growth rate enhancement due to collisions (dashed lines), along with scaling exponents α_ν (solid and dotted lines). While for $k_y \to k_x$ (upper), the scaling exponent $\alpha_\nu = 1/2$ holds very precisely (red squares), the $\alpha_\nu = 1/6$ prediction for small k_y (lower, red stars) fails to reproduce the simulation data. Instead, a value of $\alpha_\nu = 1/3$ (red diamonds) appears to describe the scaling rather well.

With $\alpha_\nu(k_y \to 0) \sim \alpha_\nu(k_y \to k_x)$, only a small shift of the spectral peak of the reconnection rate is expected. The curves in Fig. 10 illustrate this feature.

6. Pressure gradients

The work published in Ref. 27 is based on fluid model investigations of the influence of (radial) background density gradients on the reconnection rate. It is generally found that such gradients induce drifts which, in turn, suppress reconnection modes. More specifically, Ref. 27 predicts the real frequency and growth rate modification, respectively, as

$$\omega \sim \frac{\omega_{*\rm e}}{2}\left(1 - \frac{T_{\rm i}}{T_{\rm e}}\right), \tag{28}$$

$$\gamma^2 \sim \gamma_0^2 - \left[\frac{\omega_{*\rm e}}{2}\left(1 - \frac{T_{\rm i}}{T_{\rm e}}\right)\right]^2, \tag{29}$$

with $\omega_{*\rm e}/(c_s/L_{\rm ref}) = -k_y\omega_n$. Their calculation is based on Ref. 25, and therefore, the same conditions set by Eqs. (22) and (23) apply.

Thus, for $T_{\rm i} = T_{\rm e}$, there should be no change in the growth rate. In the gyrokinetic results shown in Fig. 12, however, moderate density gradients lead to a small increase of the reconnection rate. The relative enhancement of the growth rate appears to be largely independent of k_y and thus $\omega_{*\rm e}$—moreover, the growth rate increase is observed to be independent of the ion temperature (not shown here).

Again, simulations with a slightly more realistic mass ratio were performed, with $m_{\rm e}/m_{\rm i} = 0.01$ and $\beta = \beta_{\rm tot} = 0.1$, at $T_i/T_e \ll 1$, to fulfill Eqs. (22) and (23) more accurately. Here, according to Eq. (29), $\gamma_0^2 - \gamma^2 = 2.5 \times 10^{-5}$ for $k_y = 0.08$, whereas the simulation yields a value of 1.6×10^{-5}. These moderate deviations are in line with quantitatively similar differences between the model and the fluid simulation results reported in Ref. 27 where they are attributed to the limitations of the theory. In particular, the sign is the same, corresponding to gradient-induced stabilization. It is expected that for even smaller mass ratios and $k_y \to 0$, even better agreement will be achieved.

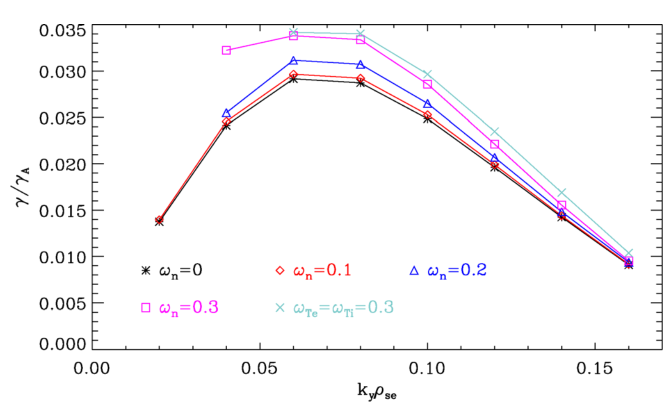

FIG. 12. (Color online) Linear growth rates in the presence of background pressure gradients. Both density gradients ω_n and temperature gradients $\omega_{Te} = \omega_{Ti}$ can be seen to have a destabilizing effect for the standard parameter set, whereas fluid theory predicts no influence of ω_n.

Again, the ω_n dependencies underscore the need for direct gyrokinetic simulations in regimes where model assumptions are not fulfilled very strictly.

At higher ω_n, the simulations yield growth rates larger by about an order of magnitude, as evidenced by the missing points at low k_y in Fig. 12. They are a consequence of the onset of fast, gradient-driven modes, which typically have a critical gradient threshold. While some of their properties survive when $v_{\text{shift}} = 0$, they are influenced by the current sheet. In either case, however, their growth rate spectra fall off continuously with k_y over the range plotted here.

Also shown in Fig. 12 are results for finite background temperature gradients (with $\omega_{Ti} = \omega_{Te}$) are found to be nearly identical in their impact on the reconnection rate to the density gradient.

Having covered a wide range of linear physics, attention is now focused on the nonlinear, turbulent phase of reconnection simulations.

IV. NONLINEAR PHYSICS

In the present work, the "linear" drive acts through the Vlasov nonlinearity. This section, however, focuses on the phase of the simulations when these modes have saturated. Here, field amplitudes and magnetic topology are of primary interest, rather than typical nonlinear observables such as heat and particle fluxes.

While in the linear section of this work, growth rates were normalized to $\gamma_A \propto B_{y0,max}$, nonlinear perturbed quantities in GENE normalization contain a factor of ρ_s/L_{ref}. It can be replaced by

$$\frac{\rho_s}{L_{\text{ref}}} = \frac{v_{\text{A}}}{c_s}\left(\frac{\beta}{2}\right)^{1/2}\frac{\sqrt{n_{e0}m_{\text{i}}}}{B_{y0,\max}}, \tag{30}$$

in order to scale amplitudes with the drive strength. Here, v_{A} is the Alfvén velocity.

In the following, results of both decaying and driven turbulence are presented.

A. Decaying turbulence

In the case of decaying turbulence, the energy injected into the system through the current sheet initial condition is simply redistributed: all terms in the Vlasov equation are turned off except for the nonlinearity, and thus no physical or numerical sinks or sources are present in the system.

An exemplary time evolution of decaying reconnection turbulence is shown in Fig. 13, where the two field components $B_{x,y}$ derived from $A_\parallel$ are evolving through the linear, nonlinear, and final stage.

The simulations in this section employ the standard physical parameters from the linear studies, with $T_{\text{i}} = T_{\text{e}}$ and $N_{\text{xp}} = 10$; while the numerical settings are chosen as follows for the data presented here: $L_{x,y} = 100\pi$, $N_x = 1024$, and $N_y = 128$.

In Fig. 14, contours of $A_\parallel$ show the temporal dynamics of the magnetic structure: the initial condition (top left) creates an instability (top right) which then leads to a brief turbulent phase (bottom left) that ultimately—once $|A_\parallel|^2$ has cascaded

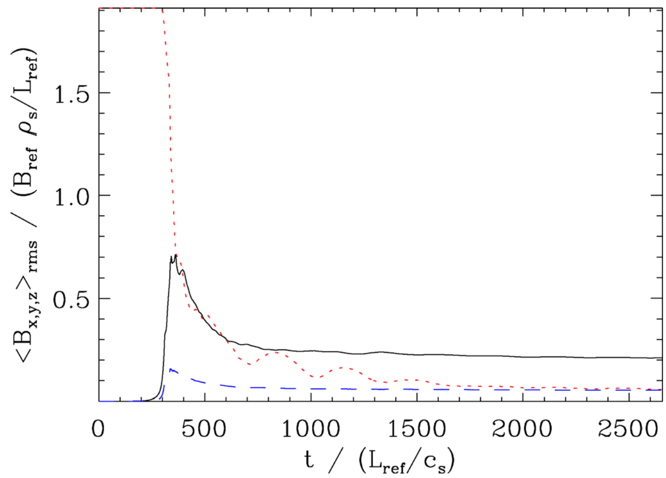

FIG. 13. (Color online) Magnetic field amplitudes for decaying turbulence: B_x (black solid line), B_y (red dotted line), and $B_\parallel$ (blue dashed line). For a description of the different phases, see the text.

inversely to the largest scales—ends up in a quiescent state (bottom right). It should be noted that the precise structure of the final state depends on numerical settings like the box size and also resolution (as resolution may change linear growth rates). Thus, the only physical aspect to be gleaned from it is the fact that $|A_\parallel|^2$ cascades to the largest scales, regardless of whether the final picture exhibits horizontal or vertical structures.

During the entire turbulent and quiescent periods, the spectra of $A_\parallel$ and Φ were found to change very little. More specifically, while—in accordance with the structural changes in Fig. 14—the large-$k_\perp$ end undergoes some adjustment, the range $k_{x,y} \sim 0.1$–1 is described very well by the following scalings: $|A_\parallel|^2 \propto k_{x,y}^{-11/3}$ and $|\Phi|^2 \propto k_{x,y}^{-10/3}$. An extension of the work published in Ref. 28 to electromagnetic turbulence should be able to recover these exponents.

The distribution function evolves from the initial sinusoidal perturbation to a more complex structure, as evidenced in Fig. 15. This structure still contains significant velocity space inhomogeneity, and while it is relatively stable in the context of a gyrokinetic simulation, it may be susceptible to other, fully kinetic instabilities such as the two-stream mechanism[29] that are not captured by the physical model employed in this work.

One of the foremost reasons why magnetic reconnection is receiving attention in the context of astrophysical phenomena lies in the fact that through the creation of strong electric fields, reconnection can provide an efficient mechanism for particle acceleration. Therefore, it is important to quantify this property for the present cases. As these simulations involve strong parallel magnetic guide fields, the primary candidate for particle acceleration is the parallel electric field.

In GENE units, $E_\parallel$ becomes

$$E_\parallel \rightarrow E_\parallel \frac{\rho_s}{L_{\text{ref}}^2}\frac{T_{\text{e}}}{e}. \tag{31}$$

Here, a hat denotes a normalized quantity. Eliminating L_{ref}, the parallel electric field normalization can be written as

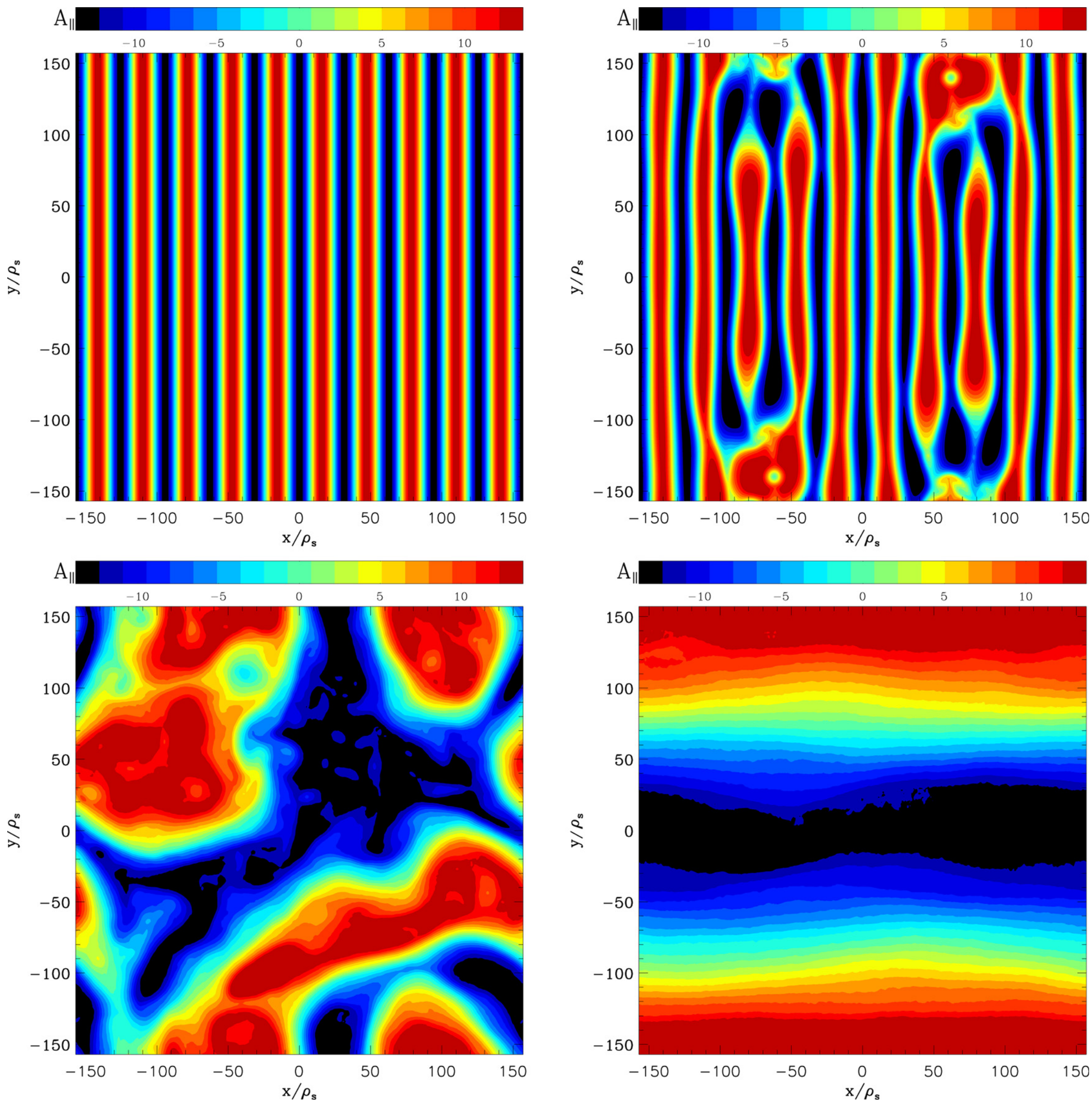

FIG. 14. (Color online) Contours of the parallel component of the magnetic potential. From the top left to the bottom right plot, the time evolution (at values $t = 0$, 310, 500, and 2659 L_{ref}/c_s) from the initial condition to the final, quiescent state is visible.

$$E_\parallel \rightarrow E_\parallel \frac{\hat{n}_{\mathrm{i}}\hat{m}_{\mathrm{i}}}{\hat{B}^2_{y0,\max}} \frac{\beta_{\mathrm{e}}}{2} \frac{v_{\mathrm{A}}^2}{c_s^2 \rho_s} \frac{T_{\mathrm{e}}}{e}, \tag{32}$$

where T_{e} is normalized to electron volts.

Since the parallel coordinate was eliminated by assuming parallel derivatives to be small, there exists no electrostatic component $E_\parallel^{\mathrm{es}} = \partial\Phi/\partial z = 0$. The electromagnetic component, however, consists of two contributions

$$E_\parallel^{\mathrm{em}} = E_\parallel^{\mathrm{fl}} + E_\parallel^{\mathrm{ind}} = \frac{1}{B_0}\mathbf{B}_\perp \cdot \mathbf{E}_\perp - \frac{\partial A_\parallel}{\partial t}, \tag{33}$$

which can be identified as a flutter and an inductive term. The former is a result of the perturbed field directing part of the perpendicular electric field along the guide field. Plotting the components of $E_\parallel = E_\parallel^{\mathrm{em}}$, one finds that while both the flutter and the inductive part contribute to the overall field, $E_\parallel^{\mathrm{fl}}$ is responsible for the lion's share, see Fig. 16. Total amplitudes range up to values of $\sim$30, with typical value during the turbulent phase lying around 10–20 (note that $B_{y0,\max} = 2.70$ in normalized units).

Looking at the field in more detail, Fig. 17 reveals that throughout the turbulent phase, filament-like structures form, again as a consequence of the flutter term. These ribbons exhibit large amplitudes of $E_\parallel$, albeit without any preferential sign when averaging over sufficiently large time windows.

From the findings in this section, it can be concluded that even the undriven gyrokinetic dissipation of a current sheet is able to produce reasonably large parallel electric fields before dying down and ending up in a non-turbulent final state.

B. Driven turbulence

With the properties of decaying turbulence in mind, simulations are performed where the drive through the initial condition is maintained through the Krook-type term in the Vlasov equation. The energy injected this way is then

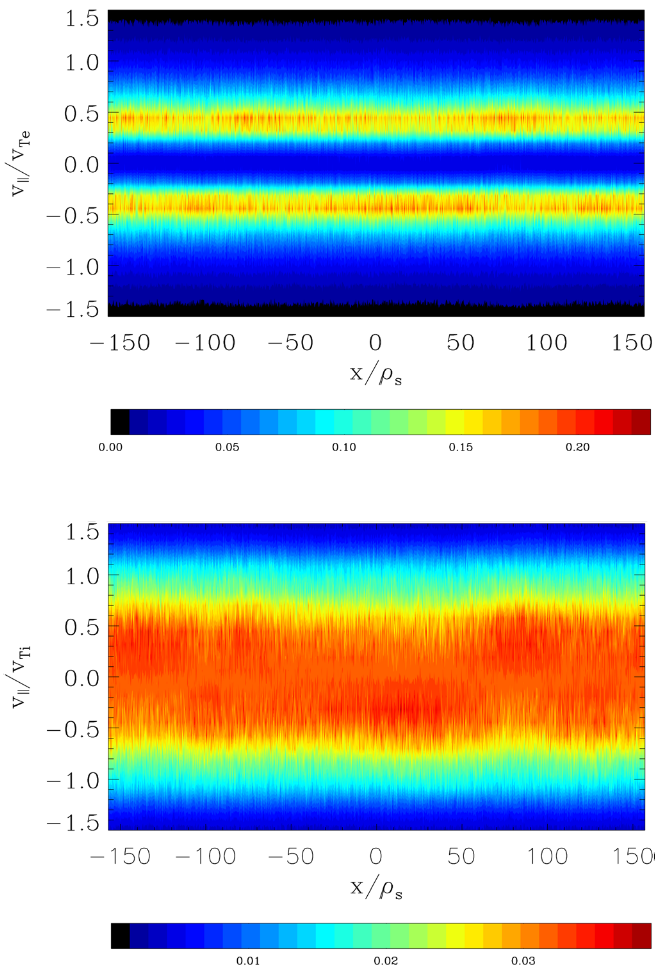

FIG. 15. (Color online) Contours of the squared perturbed part of the distribution function (above: electrons and below: ions) in the $x - v_{\|}$ plane. The remaining dimensions have been averaged over. For the above plots, the distribution data at the end of the simulation ($t = 2659\ L_{\rm ref}/c_s$) was used.

dissipated at small scales in $v_{\|}$ space through the corresponding hyperdiffusion term, which essentially mimics the effect of collisions, but is more computationally efficient. With the energetics now involving sources and sinks, this setup allows for studying quasi-stationary turbulence and the associated saturation levels of various quantities of interest. At the same time, it makes interpretation of the results more complicated, however, by introducing two additional free parameters: a drive frequency $\omega_{\rm Kr}$ and a dissipation coefficient $\epsilon_{v\|}$.

Differing in its numerical requirements from the decaying case, the simulations shown in this section resolve each radial cosine period with typically $N_x/N_{\rm xp} = 128$ and the y space with $N_y = 128$, with a box $L_x = 20\pi$ and $L_y = 50\pi$. As two cases, $N_{\rm xp} = 2$ and $N_{\rm xp} = 4$ are investigated, the base k_x of the current sheet is 0.2 and 0.4, respectively. It turns out that these cases differ not in the structures forming but rather in the amplitudes: contrary to the linear expectations, the higher k_x results in lower amplitudes (of the quantities $\mathbf{B}$ and $E_{\|}$) by a factor of about 2.5–5, while $B_{y0,\max}$ is lower by a factor of only about 2 for the higher k_x case.

The hyperdiffusion ranges from $\epsilon_{v\|} = 0.001$ to 0.02; its precise value shows relatively little impact on the turbulence—only at large times, it can play an important role, when the energy from the Krook term may not be dissipated at a sufficient rate. Such long-term behavior can, therefore, be unphysical for certain parameter settings.

As can be seen in Figs. 18 and 19, it is primarily the sources and sinks that are governing the dynamics of the system: increasing $\omega_{\rm Kr}$ by an order of magnitude causes the large-scale structures to disappear while only small islands remain, focusing the magnetic energy into relatively confined regions. This change is accompanied by an increase of $B_{\|}$ and $E_{\|}$ by a factor of 5 (for the latter, see Fig. 20); whereas $B_{x,y}$ show more complicated behavior. In the initial turbulent phase at

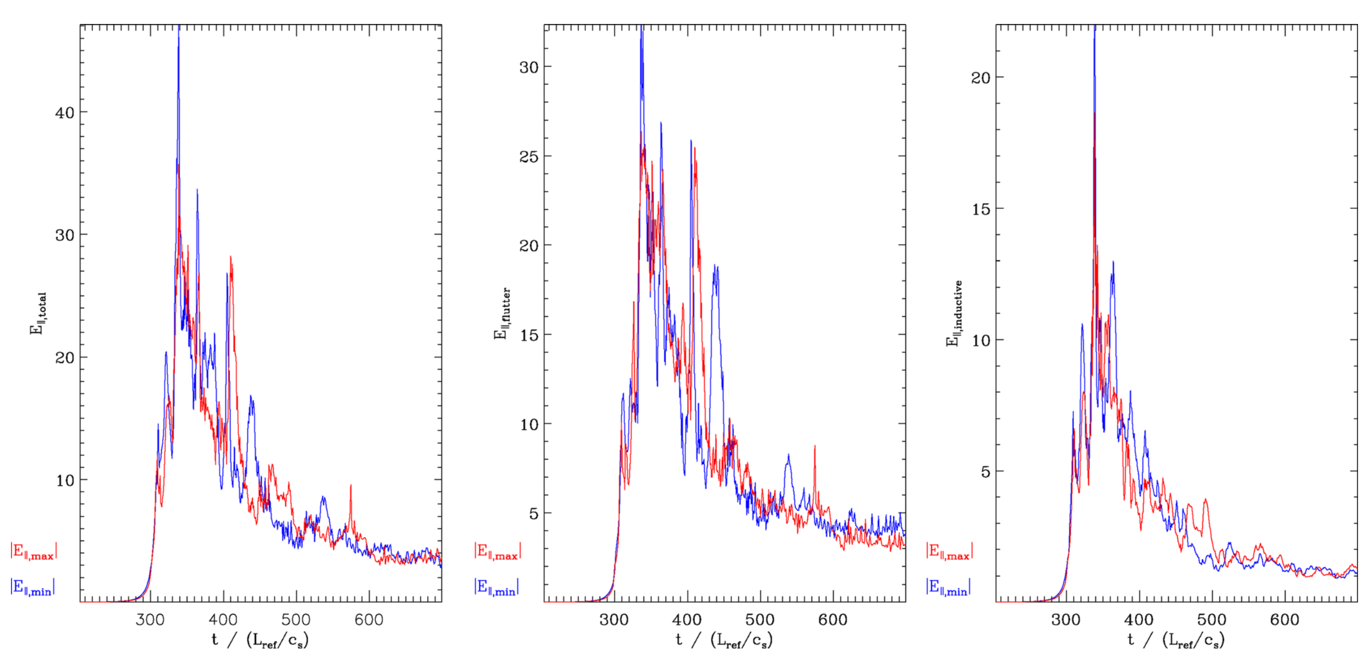

FIG. 16. (Color online) Time evolution of the parallel electric field: from left to right, the minimal (blue) and maximal (red) values of $E_{\|}^{\rm tot}$, $E_{\|}^{\rm fl}$, and $E_{\|}^{\rm ind}$ are shown, respectively. In all cases, the minimal and maximal values are of very similar amplitude, suggesting there is, on average, no preferential direction of particle acceleration.

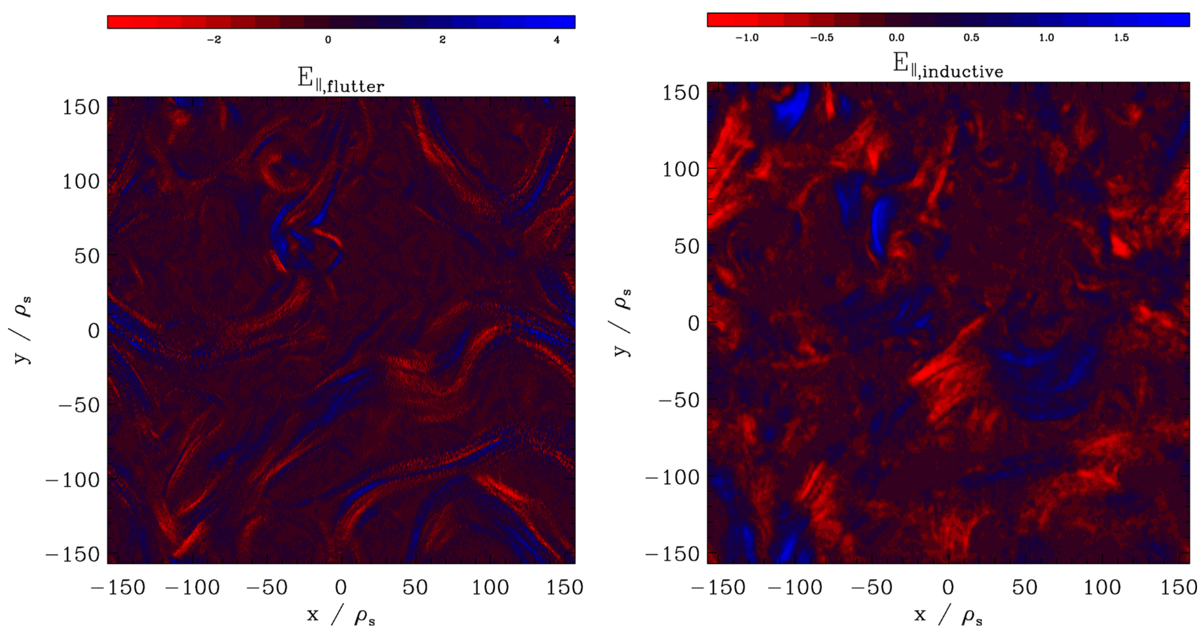

FIG. 17. (Color online) Contours of $E_{\|}^{\mathrm{fl}}$ (left) and $E_{\|}^{\mathrm{ind}}$ (right) at time $t = 500\, L_{\mathrm{ref}}/c_s$—i.e., during the turbulent phase—in the case of decaying turbulence.

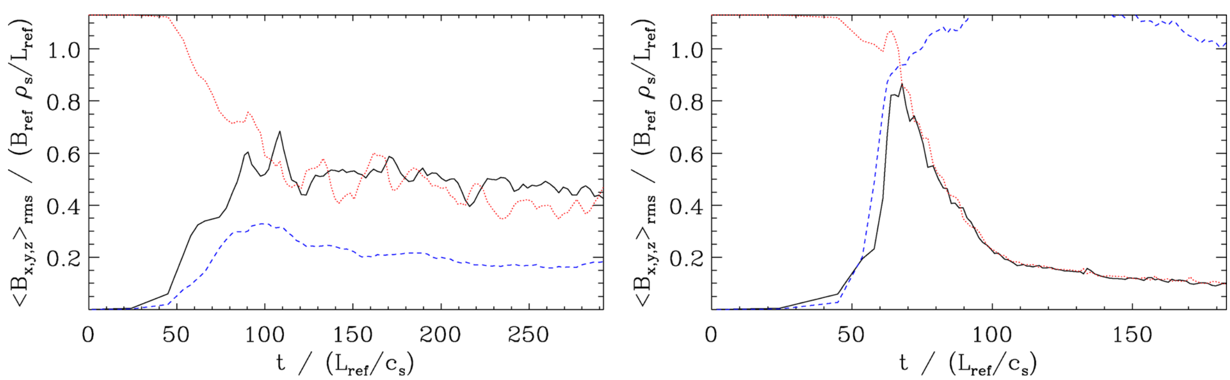

FIG. 18. (Color online) Magnetic field amplitudes for driven turbulence (left: weak drive, $\omega_{\mathrm{Kr}} = 0.01$ and right: strong drive, $\omega_{\mathrm{Kr}} = 0.1$). The black solid line corresponds to B_x, the red dotted line to B_y, and the blue dashed line to $B_{\|}$.

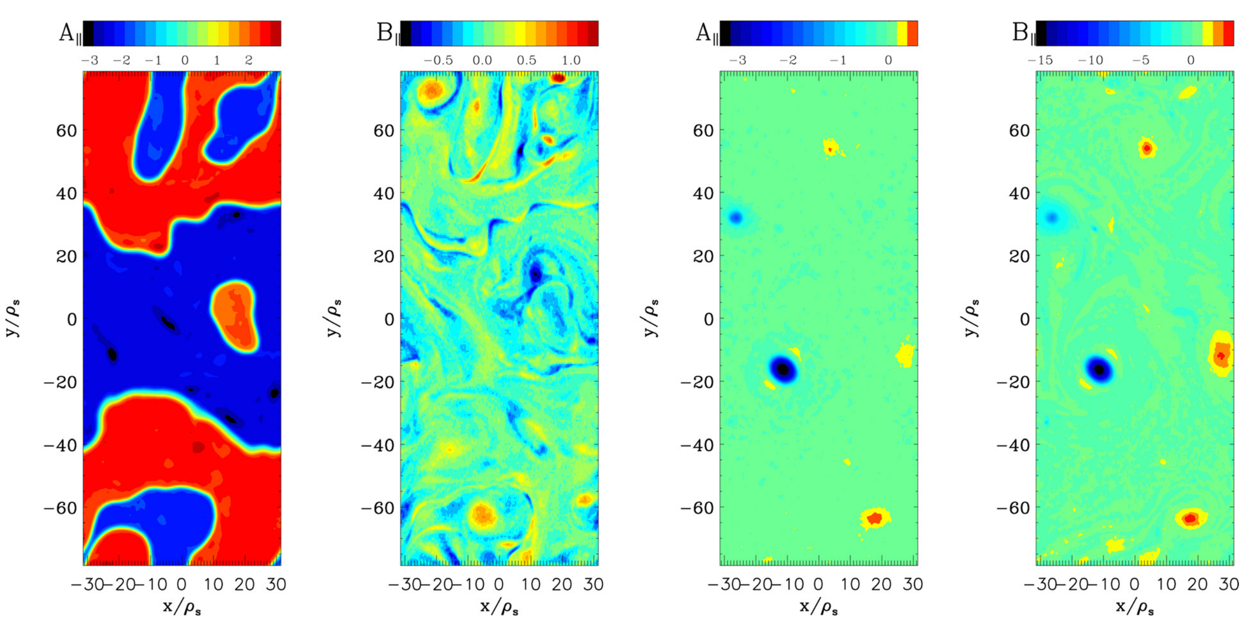

FIG. 19. (Color online) Contours of $A_{\|}$ and $B_{\|}$ for the weak (above) and strong (below) drive cases. In the former, large structures form during the quasi-stationary state, whereas the latter exhibits small islands.

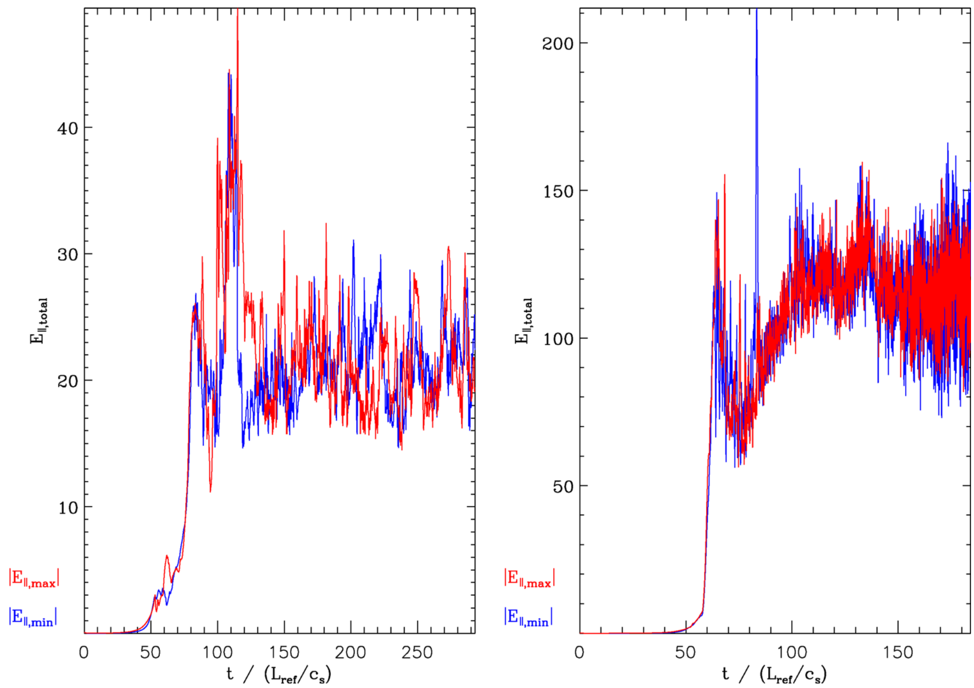

FIG. 20. (Color online) Time evolution of the parallel electric field: the minimal (blue) and maximal (red) values of $E_{\parallel}^{\text{tot}}$ are shown for the weak (left) and strong (right) drive cases. As with decaying turbulence, no preferential direction of particle acceleration is found when averaging over time.

high ω_{Kr}, their amplitude is comparable with that of $B_{\parallel}$, whereas later—when the island formation is complete—they drop off by nearly an order of magnitude. Conversely, at low drive, they saturate at roughly twice the $B_{\parallel}$ value. Note that in both cases, B_x and B_y achieve near-equipartition throughout the respective turbulent phases, as is illustrated in Fig. 18.

One simulation was performed with β reduced from the standard value of 0.3 to 0.1. It was observed that this change caused $B_{x,y}$ to drop by nearly an order of magnitude, while $B_{\parallel}$ and $E_{\parallel}$ were reduced by factors of around 3 and 15, respectively (with $B_{y0,\max}$ reduced by a factor of 3); not unlike in the previous case where modifying the perturbation

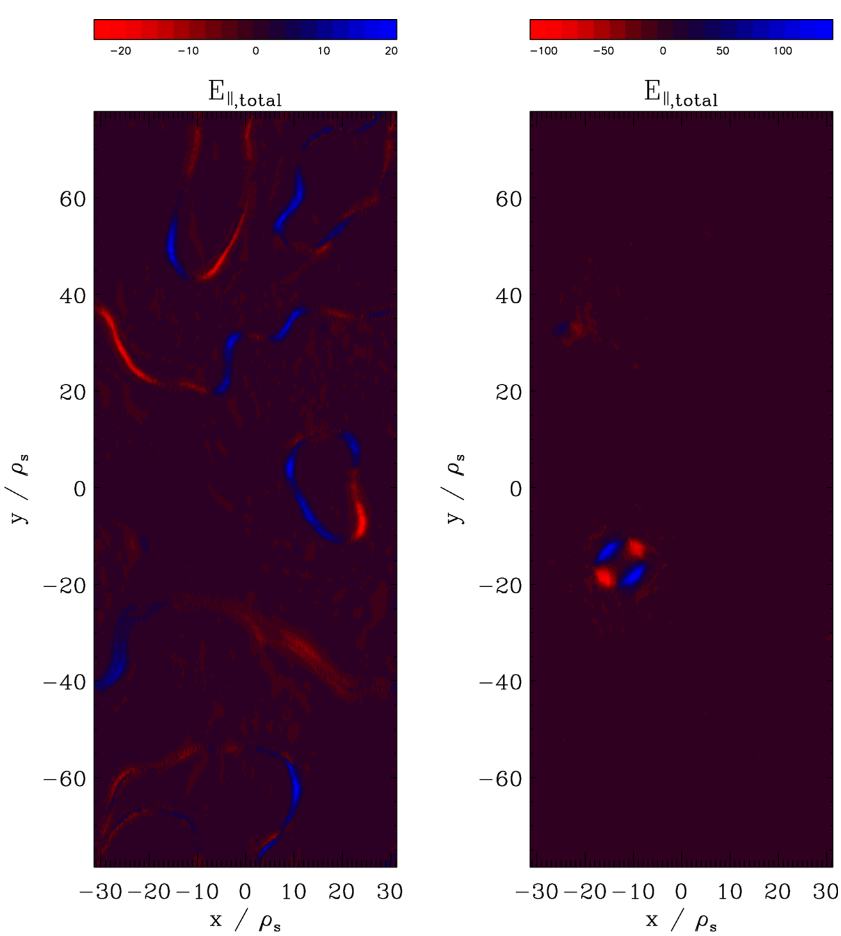

FIG. 21. (Color online) Parallel electric field contours (left: weak drive and right: strong drive) during the saturated phase ($t = 293$ and 184, respectively). The $E_{\parallel}$ structures reflect those of the magnetic potential $A_{\parallel}$, see Fig. 19.

k_x led to significant amplitude changes but virtually no qualitative changes in the topologies, reducing β had little impact on the island structures.

As in the decaying turbulence case, $E_\parallel$ is found to exhibit no preferential direction: the minimal and maximal values shown in Fig. 20 oscillate about the same mean; also, the flutter component $E_\parallel^{\rm fl}$ is again responsible for most of the total $E_\parallel$. This is in accordance with the corresponding $E_\parallel$ contours in Fig. 21 which illustrate how the parallel electric field is indeed reliant on $A_\parallel$ as shown in Fig. 19. The amplitudes of the parallel electric field depend significantly on the physical parameters such as β, $k_{x,\rm pert}$, and $\omega_{\rm Kr}$. Typical values exceed those found for the decaying case by up to an order of magnitude (at comparable $B_{y0,\max}$).

While the amplitude spectra of the direct quantities Φ and $A_\parallel$ for the simulations presented here fall off very well, it should be noted that, in particular, $E_{x,y} \sim k_{x,y}\Phi$ have very flat spectra for $k_\perp \gtrsim 1$; more specifically, the spectral slopes of $k_\perp|\Phi|^2$ and $k_\perp|A_\parallel|^2$ for the driven case agree rather well with the simulation results in Ref. 30. This highlights a somewhat problematic property of the parallel electric field: as the (dominant) flutter component of the latter depends on $E_{x,y}$, it can become difficult to resolve $E_\parallel$ down to the smallest scales. In cases where significant contributions to $E_\parallel$ stem from the high-$k_\perp$ regime, simulations can be very expensive, as very high resolutions in the perpendicular plane are necessary to sufficiently resolve all features.

V. CONCLUSIONS

The gyrokinetic reconnection studies presented in this work have covered the entire relevant parameter space linearly, and distinguished two nonlinear scenarios: decaying and driven reconnection turbulence. The linear results show that many dependencies are captured correctly by a standard fluid model; exceptions to this rule are the growth rate enhancement due to collisions and high-$k_\perp$ scenarios where FLR effects become important. Contrary to previous findings, the model describes the influence of finite ion temperature correctly, but only if mass ratio and $\beta_{\rm tot}$ obey the model assumptions in Eqs. (22) and (23) very strictly. Thus, in many realistic situations, numerical simulations are required to obtain correct reconnection rates.

Nonlinearly, a magnetic inverse cascade causes isotropization in the case of decaying turbulence, where only the initial energy from the current sheet is available to cause (quasi-) turbulent behavior. Still, significant parallel electric fields can be created through this mechanism. Even higher fields—at least by an order of magnitude—may be obtained, however, through driven reconnection. In this scenario, with a Krook term driving the turbulence, structures and islands form, with their properties depending significantly on the drive strength.

The numerically challenging nature of nonlinear gyrokinetic reconnection simulations currently makes wide-ranging multi-dimensional parameter studies of reconnection turbulence impossible. Therefore, additional investigations covering larger areas of parameter space will have to be undertaken once they become feasible. Independently, attempts should be made to extend the validity range of analytical models in order to be able to describe the physics of systems like the solar corona more accurately.

ACKNOWLEDGMENTS

This work was supported by the Max Planck Society through the Interinstitutional Research Initiative "Turbulent transport and ion heating, reconnection, and electron acceleration in solar and fusion plasmas," Project No. MIF-IF-A-AERO8047. Additionally, the authors would like to thank B. N. Rogers, R. Numata, T. Görler, H. Doerk, A. Biancalani, W. Dorland, and J. Lee for their help and valuable discussions.

[1] E. N. Parker, J. Geophys. Res. **62**, 509, doi: 10.1029/JZ062i004p00509, (1957).
[2] P. A. Sweet, in *Electromagnetic Phenomena in Cosmical Physics*, edited by B. Lehnert (Cambridge University Press, New York, 1958), p. 123.
[3] P. A. Cassak, M. A. Shay, and J. F. Drake, Phys. Rev. Lett. **95**, 235002 (2005).
[4] D. Grasso, E. Tassi, and F. L. Waelbroeck, Phys. Plasmas **17**, 082312 (2010).
[5] A. Perona, L.-G. Eriksson, and D. Grasso, Phys. Plasmas **17**, 042104 (2010).
[6] R. Fitzpatrick, Phys. Plasmas **17**, 042101 (2010).
[7] D. Del Sarto, C. Marchetto, F. Pegoraro, and F. Califano, Plasma Phys. Controlled Fusion **53**, 035008 (2011).
[8] A. Biancalani and B. D. Scott, "Observation of explosive collisionless reconnection in 3D nonlinear gyrofluid simulations," Europhys. Lett. (submitted).
[9] T. Matsumoto, S. Tokuda, Y. Kishimoto, T. Takizuka, and H. Naitou, J. Plasma Fusion Res. **75**, 1188 (1999).
[10] W. Wan, Y. Chen, and S. E. Parker, Phys. Plasmas **12**, 012311 (2005).
[11] B. N. Rogers, S. Kobayashi, P. Ricci, W. Dorland, J. Drake, and T. Tatsuno, Phys. Plasmas **14**, 092110 (2007).
[12] X. Y. Wang, Y. Lin, L. Chen, and Z. Lin, Phys. Plasmas **15**, 072103 (2008).
[13] E. A. Frieman and L. Chen, Phys. Fluids **25**, 502 (1982).
[14] T. S. Hahm, W. W. Lee, and A. Brizard, Phys. Fluids **31**, 1940 (1988).
[15] A. Brizard, J. Plasma Phys. **41**, 541 (1989).
[16] F. Merz, Ph.D. thesis, University of Münster, 2009.
[17] See http://gene.rzg.mpg.de for code access and documentation.
[18] M. J. Pueschel, T. Dannert, and F. Jenko, Comput. Phys. Commun. **181**, 1428 (2010).
[19] X. Lapillonne, B. F. McMillan, T. Görler, S. Brunner, T. Dannert, F. Jenko, F. Merz, and L. Villard, Phys. Plasmas **17**, 112321 (2010).
[20] A. B. Navarro, P. Morel, M. Albrecht-Marc, D. Carati, F. Merz, T. Görler, and F. Jenko, Phys. Plasmas **18**, 092303 (2011).
[21] B. N. Rogers, private communication (2010).
[22] E. G. Harris, Nuovo Cimento **23**, 115 (1962).
[23] B. N. Rogers, S. Kobayashi, P. Ricci, W. Dorland, J. Drake, and T. Tatsuno, Phys. Plasmas **18**, 049902 (2011).
[24] R. Numata, G. G. Howes, T. Tatsuno, M. Barnes, and W. Dorland, J. Comput. Phys. **229**, 9347 (2010).
[25] F. Porcelli, Phys. Rev. Lett. **66**, 425 (1991).
[26] H. P. Furth, J. Killeen, and M. N. Rosenbluth, Phys. Fluids **6**, 459 (1963).
[27] E. Tassi, F. L. Waelbroeck, and D. Grasso, J. Phys. Conf. Ser. **260**, 012020 (2010).
[28] G. G. Plunk, S. C. Cowley, A. A. Schekochihin, and T. Tatsuno, J. Fluid Mech. **664**, 407 (2010).
[29] E. S. Weibel, Phys. Rev. Lett. **2**, 83 (1959).
[30] G. G. Howes, W. Dorland, S. C. Cowley, G. W. Hammett, E. Quataert, A. A. Schekochihin, and T. Tatsuno, Phys. Rev. Lett. **100**, 065004 (2008).